Geophysical Research Letters®

RESEARCH LETTER
10.1029/2021GL095838

Key Points:

- Seismic low-velocity zones (LVZs) are observed above and below the mantle transition zone (MTZ) surrounding the Yellowstone hotspot
- The Yellowstone plume and Farallon slab may displace hydrous MTZ rock to release water via mineral phase change to cause the LVZs
- The weak LVZ directly above the Yellowstone plume suggests that ascending rock is relatively dry, consistent with a lower-mantle upwelling

Supporting Information:

Supporting Information may be found in the online version of this article.

Correspondence to:

W. D. Frazer,
william.frazer@yale.edu

Citation:

Frazer, W. D., & Park, J. (2021). Seismic evidence of mid-mantle water transport beneath the Yellowstone region. *Geophysical Research Letters*, *48*, e2021GL095838. https://doi.org/10.1029/2021GL095838

Received 2 SEP 2021
Accepted 30 SEP 2021

Seismic Evidence of Mid-Mantle Water Transport Beneath the Yellowstone Region

William D. Frazer[1] and **Jeffrey Park**[1]

[1]Department of Earth and Planetary Sciences, Yale University, New Haven, CT, USA

Abstract Earth's mantle transition zone (MTZ) is a possible global water reservoir and may be responsible for long-term (~100 Ma) ocean-mass regulation. Estimates of water capacities in MTZ minerals are ~1 wt%, far greater than that of rocks of the surrounding mantle. When water-rich material is displaced from the MTZ, partial melting occurs, generating a sharp reduction in seismic velocities detectable with seismic receiver functions (RFs). We estimated RFs for the MTZ beneath the Yellowstone region using earthquakes recorded by ~200 stations of the Earthscope Transportable Array. We found many LVZs both above and below the MTZ, consistent with water release upon phase transformation of hydrated MTZ rock into upper- and lower-mantle mineral assemblages with low water capacities. The locations of LVZs are consistent with mid-mantle flow induced by descent of a Farallon-slab fragment and ascent of the deeply rooted Yellowstone plume as imaged by seismic tomography.

Plain Language Summary The Earth's mantle transition zone, located at 410–660 km depth, has been identified as a possible global water reservoir, responsible for regulating the mass of Earth's oceans over geologic time. Water is transported in hydrated minerals to the transition zone by the subduction of plates and it is returned to the oceans by plumes. Transition zone rock has a water-storage capacity of ~1.0 wt%. Upper- and lower-mantle rock has a much lower capacity for water, on the order of 0.1 wt%. Due to the significant discrepancy in water-storage capacity, when hydrated minerals leave the transition zone, the rock partially melts. Sharp boundaries associated with partial-melt layers can reduce the velocities of seismic waves by a few percent, which is detectable using seismic waves that convert at the interface between rock with and without partial melt. The Yellowstone region provides an opportunity to seek hydrous partial melting above and below the transition zone because both a subducting slab and an upwelling plume are thought to be present. The pattern of low-velocity layers detected underneath Yellowstone is consistent with the expected rock flow for a plume that originates within the lower mantle.

1. Introduction

The hydration potential of Earth's mantle transition zone (MTZ) may be responsible for long-term (~100 Ma) ocean-mass regulation, driven by plate tectonics and mantle convection (Bercovici & Karato, 2003; Karato et al., 2020). Constraining the solid-Earth water cycle over geologic time is key in understanding the volatile-compound budget and planetary habitability (Langmuir & Broecker, 2012). Minerals within the MTZ, primarily wadsleyite and ringwoodite, are able to store 1–3 wt% of water (Kohlstedt et al., 1996), far greater than minerals in the upper or lower mantle. Typical upper-mantle rock is estimated to have a maximum water content of ~0.1 wt% from mid-ocean ridge basalts and a water storage capacity of ~0.1 wt% (Hirschmann, 2006; Saal et al., 2002). The lower-mantle is estimated to have similarly low water capacity (Bolfan-Casanova, 2005). High water capacity does not necessarily imply high water content, but some deep xenoliths provide evidence for a hydrous MTZ. Water-rich diamond inclusions have been found with water content of 1.4 wt% (Pearson et al., 2014) and ice VII inclusions (Tschauner et al., 2018). Electrical conductivity measurements have also supported high water content in the MTZ, with large regional variations (Karato, 2011). The combination of high-water storage capacity and geologic evidence suggest the MTZ is a key component of the solid-Earth water cycle.

When water-rich material from the transition zone penetrates the upper or lower mantle, partial melting occurs due to the decrease in water capacity after phase transition, generating a seismic low-velocity zone (LVZ). In order for melt to generate low-velocity anomalies, grain-boundaries must wet significantly (Yoshino et al., 2007). Such LVZs have been detected above and below the MTZ, and have been interpreted as displaced hydrous material (Liu et al., 2016, 2018; Song et al., 2004; Tauzin et al., 2010). Above the 410-km discontinuity, melts are expected to pool since wet melt is generally more dense than upper-mantle rock (Jing & Karato, 2012). The LVZs below the 660-km discontinuity are observed roughly 100 km below the MTZ, in the 730–800-km depth range. It has been proposed that water can be transported to this depth by either metallic iron (Liu et al., 2018) or garnet (Panero et al., 2020) before release into the surrounding lower-mantle mineral assemblage. In the deep Japan subduction zone, an LVZ located above the MTZ has been detected using seismic tomography (Zhao & Ohtani, 2009), travel-time triplications (Han et al., 2021), and receiver functions (Liu et al., 2016; Wang et al., 2020). Additionally, Liu et al. (2016) imaged an LVZ at ~750 km, directly below the Japan slab. Wet upwelling and an LVZ above the Japan Slab have been suggested as the source for Changbaishan volcanism in NE Asia (Yang & Faccenda, 2020; Zhao & Ohtani, 2009).

The Yellowstone hotspot is another instance of inter-plate volcanism with an enigmatic origin. It has been suggested that an upper-mantle source may be responsible for the hotspot (e.g., Christiansen et al., 2002), but more recent seismic tomography suggests a deeply rooted plume (e.g., Nelson & Grand, 2018). The remnant Farallon slab has been imaged to the southwest of the hotspot (James et al., 2011; Schmandt & Lin, 2014), but it is not visible in every tomographic model (Schmandt et al., 2012). Dynamics of the remnant slab are thought to be complicated, including slab fragmentation (e.g., Long, 2016) and possible reverse subduction at transition-zone depths (Zhou, 2018). Previous low-frequency (~0.25 Hz) receiver function (RF) studies have found an LVZ above the 410-km discontinuity in the western United States (Fee & Dueker, 2004; Hier-Majumder & Tauzin, 2017; Schmandt et al., 2011; Tauzin et al., 2010), and a complex pattern of apparent interfaces within the upper mantle (Eagar et al., 2010; Gilbert et al., 2003). An LVZ below the 660-km discontinuity has been identified in RF profiles to the east of the hotspot (Schmandt et al., 2014). Higher-frequency RF analysis can provide finer vertical resolution and help elucidate complicated structure. The combination of possible upwelling and downwelling in the mid-mantle surrounding the Yellowstone hotspot provides an opportunity to search for hydrous melting above and below the MTZ.

In this study, we stack multiple-taper correlation (MTC) RFs (Park and Levin, 2000, 2016) below the Yellowstone hotspot. High frequencies can be used because multiple-taper RF estimates, which reduce the effects of spectral leakage (Park et al., 1987), can be stacked with uncertainty weighting. We obtained ~21,000 waveforms from the Incorporated Research Institutions for Seismology (IRIS) Data Management Center (DMC) for RF analysis. Using common conversion point (CCP) RF-stacks (Bianchi et al., 2010; Dueker & Sheehan, 1997), we estimated RFs on an equally spaced grid in the Yellowstone region, using moving-window moveout corrections to target specific depth ranges.

2. Data and Method

2.1. Data

We used seismic data recorded by ~200 stations within 5° of the Yellowstone caldera from the EarthScope Transportable Array (TA) (IRIS Transportable Array, 2003), obtained via ObsPy (e.g., Krischer et al., 2015) from the IRIS DMC. Using waveforms recorded on one dense network allows for consistent data quality and coverage. After visual inspection, we analyzed 20,923 waveforms from earthquakes of magnitude $M \geq 6.0$ and epicentral distance $30° \leq \Delta \leq 99°$ with clear P-wave arrivals. All seismic records were demeaned, linearly detrended, and high passed at 0.01 Hz to avoid drift and long-period noise. P-wave arrival times were estimated with the ak135 1-D earth model (Kennett et al., 1995). We note that we include more low-frequency signal than previous studies (e.g., Liu et al., 2018; Schmandt et al., 2012), in order to reduce RF side lobes.

2.2. RF Processing and Stacking

We first rotated the horizontal components from North-East (N-E) to radial-transverse (R-T). RFs were computed in the frequency domain using the multiple-taper spectrum correlation method, allowing much higher-frequency and noisier data to be used (Park & Levin, 2000; Park et al., 1987). We set the time-bandwidth product $p = 2.5$ and selected the first three Slepian eigentapers in our spectrum estimate. Time windows were set to 90 s duration, starting 23 s prior to the prior to the predicted P-wave arrival time (vertical component) or Ps delay time (radial and transverse component) – see Figure S6 in the Supporting Information S1.

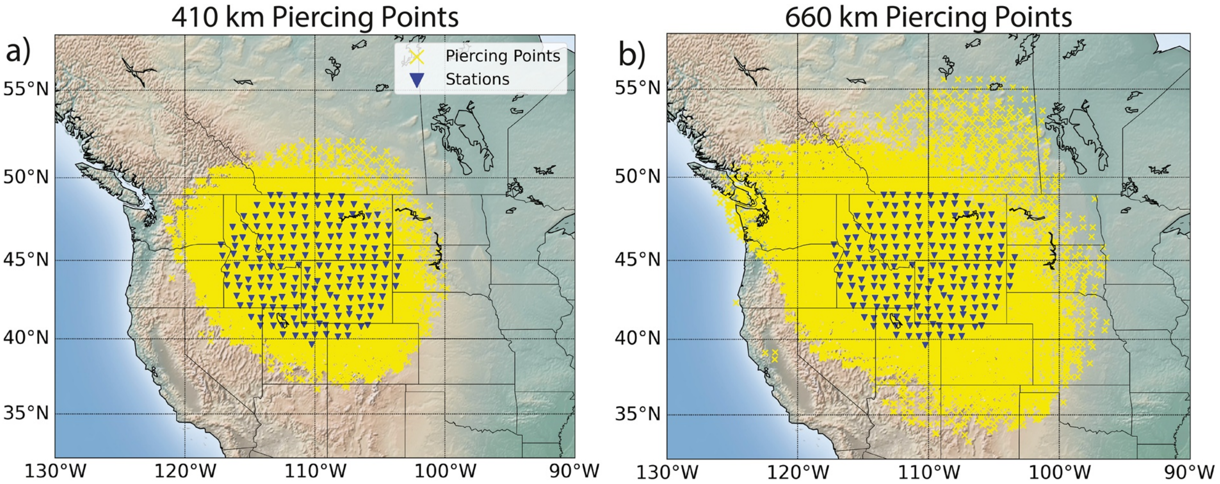

Figure 1. Maps of piercing points (yellow Xs) and seismic stations (blue inverted triangles) at (a) 410 km and (b) 660 km depth.

Ps delay times were calculated via ray tracing through the US-SL-2014 tomography model (Schmandt & Lin, 2014), obtained from the IRIS Earth Model Collaboration (Trabant et al., 2012).

Individual RFs were stacked using the CCP method (Bianchi et al., 2010; Dueker & Sheehan, 1997). Ray-piercing points were calculated for binning depths between 310 and 760 km in 50 km increments using the ak135 reference model (Figure 1). Piercing points were binned with overlapping 1°-radius circles with centers spaced at 0.5° between 38°N and 51.5°N and 118°W and 103.5°W, generating a total of 840 individual RFs. Stacking uncertainty is estimated with the jackknife resampling method; we consider features significant if the RF value is greater than one standard deviation. Frequency domain RFs were filtered before an inverse Fourier transform with a cosine-squared taper set at cutoff frequencies f_c selected between 0.25 and 0.65 Hz.

LVZs were identified as the minimum signal greater than one standard deviation in an RF trace near their predicted depth, ~380 and ~750 km respectively. MTZ depth was selected as the maximum RF value in a 70-km window around 410 and 660 km depth. Where double pulses characterize the MTZ interfaces, topography was set with visual inspection. The edges of each profile extend outside the station footprint, where they do not have crossing ray paths and results are less reliable. LVZs, the 410-km, and 660-km discontinuity were identified using $f_c = 0.65$ Hz. RFs with lower cutoff frequencies were computed to confirm interpretations at 0.65 Hz. All calculations were made in Python using the ObsPy package (e.g., Krischer et al., 2015).

3. Results

We summarize our calculations in Figures 2 and 3. The topography of the 410- and 660-km discontinuities along with MTZ thickness is shown in Figure 2. The locations of LVZs above and below the MTZ are shown in Figure 3. A representative RF CCP is shown in Figure 3c.

3.1. Above the 410-km Discontinuity

Across our RF grid, the 410-km discontinuity appears as a single positive pulse even at frequency cutoff $f_c = 0.65$ Hz (Figure S2 in the Supporting Information S1). A positive pulse indicates a velocity increase with depth, as is expected at the top of the MTZ. Under Montana, northern Wyoming, and eastern Idaho, the 410-km discontinuity is often depressed by ~10–20 km (~1–2 s) compared to the migration depth (Figure 2a). A similar depression is found to the southwest under northern Utah. Atop the MTZ, negative pulses with delay-time anomalies $\Delta t \sim -1$ to -5 s (~10–50 km) above the 410-km discontinuity are observed in some RFs (Figure 3a; Figure S2 in the Supporting Information S1). These features are found throughout the station footprint, but the strongest signals are concentrated directly north of the Yellowstone hotspot in central Montana and the southwestern portion of our station footprint. We interpret these features as

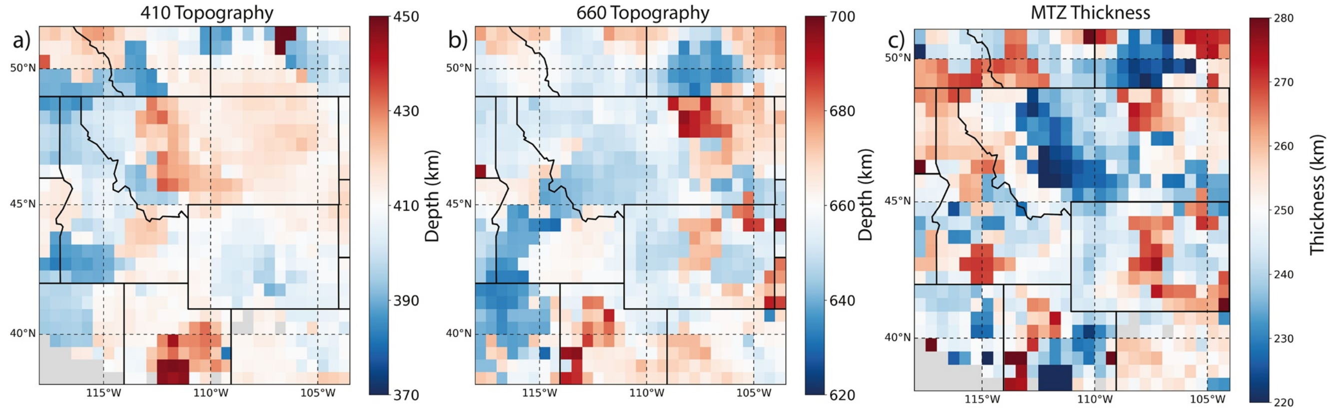

Figure 2. Maps of (a) 410-km and (b) 660-km discontinuity topography as well as (c) mantle transition zone thickness. Topography was calculated by selecting the maximum receiver function (RF) value for RFs calculated in 1° bins.

velocity inversions. In a representative CCP profile with migration depths from 360 to 460 km the negative pulses above the MTZ are robust to variations in the migration depth (Figure S4 in the Supporting Information S1). Additionally, the moveout of these Ps conversions follows that predicted for the 410-km

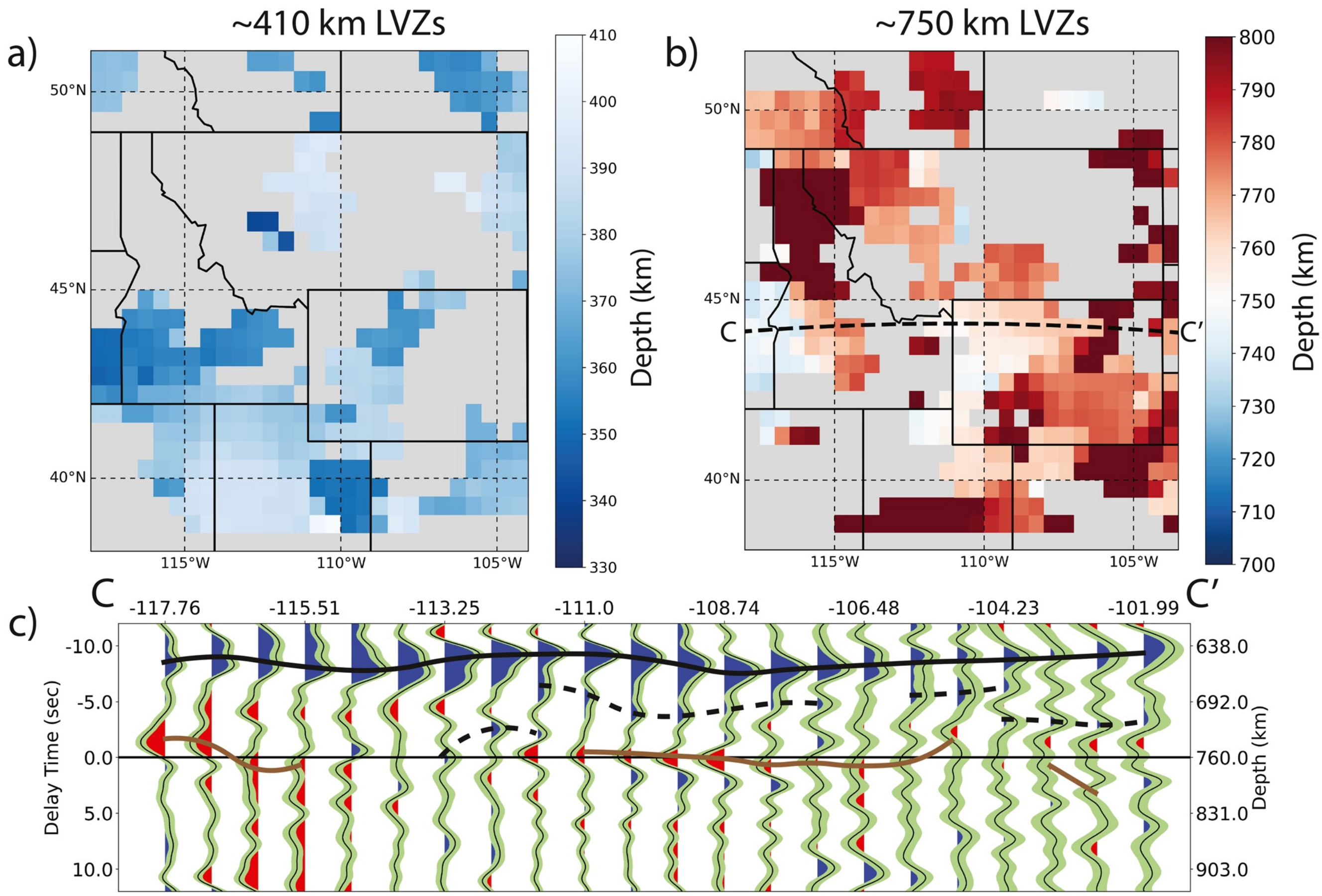

Figure 3. Depth maps of low-velocity zones (LVZs) above the (a) 410-km and below the (b) 660-km calculated on receiver functions (RFs) stacked in 1° bins. A common conversion point profile of radial RF stacks for line C-C' is shown in (c) migrated to 760 km depth. Positive RF pulses are blue and negative pulses are red. The pale-green shaded regions denote the 1-σ jackknife uncertainties. The 660-km discontinuity is marked with a solid black curve. Dotted black lines indicate possible 730-km interfaces due to high basalt content (see Section 3.2). Interpreted LVZs are marked with brown curves. LVZs were identified at $f_c = 0.65$ Hz.

discontinuity (Figure S6 in the Supporting Information S1), and not multiples from shallow structure. We find that an increase in cutoff frequency increases the number of apparent LVZs in images above the 410-km discontinuity. For example, the negative pulses observed in Figure S2c in the Supporting Information S1 can only be observed when $f_c \geq 0.5$ Hz. Figure 2a shows the geographic extent of the depressed 410-km discontinuity and Figure 3a shows the LVZs above the MTZ. Although too shallow for our interpretation, we note the presence of positive Ps at ~300–370 km in many RFs, consistent with a positive jump in seismic velocity within the upper mantle (Figure S2 in the Supporting Information S1). A similar feature was observed in the western US (Maguire et al., 2018) and has been suggested to be a deep expression of the Lehmann discontinuity (Gilbert et al., 2003).

3.2. Below the 660-km Discontinuity

The 660-km discontinuity appears as a clear positive pulse across the study region (Figure S3 in the Supporting Information S1). Under western Montana, we find the 660-km discontinuity to shallow by ~10–20 km (~1–2 s) (Figure 2b). At low frequency (0.25 Hz) the interface appears as a wide pulse with a width between 4 to 8 s (~40–80 km), but at higher frequency (0.65 Hz) the pulse sometimes appears to split, with one pulse generally deeper (~690–740 km). This complicates the interpretation of the 660-km discontinuity and LVZs at ~750 km depth. Examples of double-pulses at the 660-km discontinuity are shown in Figure 3c and Figure S3 in the Supporting Information S1. We address this feature in the Discussion. To the northwest of the Yellowstone hotspot, the 660-km discontinuity is observed to shallow by ~2 s (~20 km). We find these pulses to be robust because they persist in RFs with migration depths from 660 to 760 km (Figure S5 in the Supporting Information S1).

Negative pulses, interpreted as LVZs, are detected below the 660-km discontinuity over much of the array (Figure 3b). We do not observe these features below north-central Montana or much of eastern Idaho and southwestern Montana. In other portions of our station footprint, the velocity inversions typically lie at ~750 km depth, but some are as shallow as ~710 km or as deep as ~800 km. In general, the LVZs observed below the MTZ can be observed with $f_c = 0.25$ Hz to $f_c = 0.65$ Hz, suggesting that they are robust. Similar to the 410-km discontinuity, the moveout of these Ps conversions follows that predicted for the 660-km discontinuity (Figure S6 in the Supporting Information S1), and not multiples from shallow structure. In the center of the station footprint, LVZs tend to be observed ~30 km shallower than in outer portions. The LVZs below the MTZ, consistent with a sinking mantle, are rarely found in the same location as a shallow 660-km discontinuity. This would be consistent with the Clapeyron-slope effect of a rising plume (Bina & Helffrich, 1994). In the southwestern edge of our station footprint, LVZs below the MTZ are located above dipping positive pulses, possibly associated with relict slabs, but these observations are not as reliable due to a lack of crossing ray paths.

4. Discussion

4.1. Geodynamic Context

The mid-mantle surrounding the Yellowstone hotspot hosts many geodynamic features, most notably a mantle plume. Although there has been considerable debate about the nature of the plume, multiple seismic tomography studies have identified its signature within the uppermost lower mantle (e.g., Schmandt et al., 2012). Recent tomography that incorporates SKS and SKKS traveltimes has deepened the plume conduit into the lowermost mantle (Nelson & Grand, 2018). Between 300 to 700 km depth tomography suggests upwelling that is focused below the Yellowstone hotspot and to the north and west (the junction of Idaho, Montana, and Wyoming). Underneath much of central Montana, a low-velocity anomaly is imaged at ~700 km depth (Nelson & Grand, 2018). In addition to the upwelling plume, there are multiple high-velocity anomalies observed on the western side of our station footprint, interpreted as subducting slabs. The primary explanation involves the remnant Farallon plate which may descend into the MTZ at the southwestern extreme of our station footprint (e.g., James et al., 2011). Combining these interpretations, upwelling at the 410-km discontinuity occurs beneath and to the north and west of Yellowstone and downwelling occurs on the western edge of the station footprint.

4.2. Seismic Observations

Where we infer mantle upwelling, we observe a depressed 410-km discontinuity, a shallowed 660-km discontinuity, and no LVZs above or below the MTZ. These observations are consistent with an upwelling dry plume. A hot plume conduit should increase the pressure at which olivine converts to wadsleyite, thus depressing the 410-km discontinuity. At the 660-km discontinuity an increase in temperature shallows the transition to lower-mantle mineralogy (Bina & Helffrich, 1994), which can also be enhanced by low water content (e.g., Ohtani & Litasov, 2006). Our model for the LVZs observed below the 660-km discontinuity involves downwelling hydrous material from the MTZ. We do not expect an LVZ to occur within the upwelling flow of the plume. Furthermore, a plume conduit consists of dry lower-mantle material. Assuming scant mixing with MTZ rock, we expect no LVZ to be present in the Yellowstone plume above the MTZ. Based on our RFs, it appears the Yellowstone conduit in the mid-mantle lies primarily below south-central Montana. Multiple tomography studies have placed the plume conduit in a similar location (James et al., 2011; Nelson & Grand, 2018; Schmandt et al., 2012). The topography of the 660-km discontinuity we observe is consistent with previous RF studies (Eagar et al., 2010; Fee & Dueker, 2004; Schmandt et al., 2012), but we find the topography of the 410-km discontinuity to be less consistent. One likely reason for this discrepancy is the high-frequency nature of our RF estimates. As cutoff frequency increases, the shape of individual pulses narrows, but does not always peak at the center of the lower frequency pulse. This can change the estimated depth of the interface and previous high-frequency RFs from the western US have exhibited similar behavior (Schmandt et al., 2011). Our RF calculations do identify the thinnest MTZ in a similar location as previous RF analysis (Figure 2c), just to the northwest of the surface hotspot (Fee & Dueker, 2004; Hier-Majumder & Tauzin, 2017; Schmandt et al., 2012).

We observe patches of LVZs above (∼380 km) and below the MTZ (∼750 km) (Figure 3). The RF amplitudes of these features fall in the range predicted by perturbations to the S wavespeed (1.3%–2.8%), all above the 1-σ jackknife-uncertainty envelope. These estimates are based only on RFs where the 410-km and 660-km discontinuities appear as single pulses, so that multipathing does not bias the Ps amplitude of the MTZ discontinuities. The precise relationship between Ps amplitude and seismic-wavespeed perturbation depends on the *P*-wave incidence angle, and therefore depends on epicentral distance for individual events. Observed LVZ RF amplitudes agree with previous studies in the western US (Hier-Majumder & Tauzin, 2017; Schmandt et al., 2011, 2012, 2014). In the Yellowstone region, the remnant Farallon plate is subducting and could displace MTZ rock as it enters from the upper mantle. This may cause hydrated MTZ material to invade both the upper and lower mantle, where conversion to a low-water-capacity mineral assemblage would generate LVZs above and below the MTZ. Liu et al. (2018) interpreted a similar scenario to operate beneath the European Alps. This mechanism fails to explain the LVZs to the north and east of the plume, where we propose that MTZ rock displaces upward within the flow field of the upwelling plume. Immediately surrounding the Yellowstone plume, the mantle flow field can entrain hydrous MTZ rock and transport it vertically through the 410-km discontinuity where partial melting can occur. In this scenario, no LVZ is found above the hotter, more-buoyant plume conduit, because dry lower-mantle rock has not mixed with, or captured water from, the surrounding MTZ rock. We summarize our geological interpretations in Figure 4.

We infer these melts above the MTZ, including those generated via viscous coupling, to be denser than the ambient lowermost upper-mantle rock (Jing & Karato, 2012). Hydrous melt above the 410-km discontinuity may become less dense than the ambient upper mantle if the water content exceeds ∼1% and the local temperature is anomalously low (Karato et al., 2020). Along these lines, a supra-410-km melt layer above the deep Japan slab has been interpreted as the source of the Changbaishan volcanism in NE Asia (Yang & Faccenda, 2020; Zhao & Ohtani, 2009). However, we do not infer this mechanism as a source of volcanism in the western US, because depressions of the 410-km discontinuity suggest a warmer adiabat and therefore dense supra-410 melt.

LVZs are not observed above the 410-km discontinuity in southwestern Montana and eastern Idaho where the mantle plume has been interpreted (James et al., 2011; Nelson & Grand, 2018; Schmandt et al., 2012). A similar gap in LVZs was found by Hier-Majumder and Tauzin (2017), but we do not observe a LVZ just to the north of Yellowstone hotspot as previously interpreted (Schmandt et al., 2011).

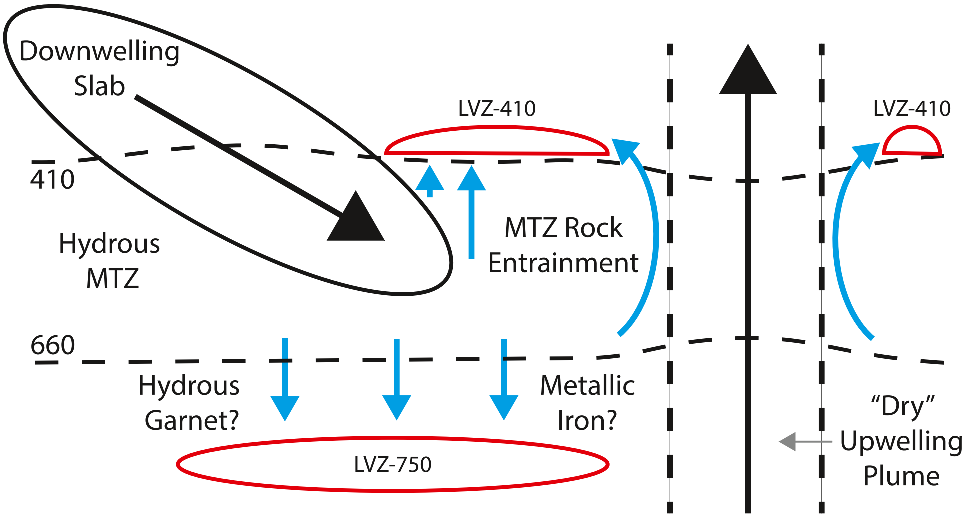

Figure 4. Schematic of the interpreted features. Dashed lines indicate either 410-km or the 660-km discontinuity. Black arrows indicate either upwelling or downwelling flow. Blue arrows show the interpreted flow of hydrous material. Low-velocity zones are marked with red ellipses.

Below the MTZ we observe LVZs at ~750 km depth in all regions where downwelling is likely due to subducting slab remnants and also to the eastern portion of our station footprint, away from the upwelling plume (Figure 3b). In northwestern Montana, we detect LVZs in agreement with previous observations, however, to the east we do not observe any LVZs (Schmandt et al., 2014). Additionally, no LVZs are detected in north-central Montana, where low velocities have been predicted by seismic tomography (Nelson & Grand, 2018). The interpretation of LVZs below the 660-km discontinuity is complicated by positive signals observed in the RFs just below the MTZ, resulting in a double pulse. High-frequency RFs from previous work in the region have exhibited similar characteristics (Schmandt et al., 2011). A double pulse may be the result of 3-D structure that is not corrected by the tomography model used to perturb Ps delay times from a 1-D velocity profile. However, previous similar seismic observations of LVZs at ~700–750 km depth have been interpreted as the transition of garnet to bridgmanite (e.g., Deuss et al., 2006; Simmons & Gurrola, 2000). A sharp interface at these depths has been suggested to be evidence of high basalt content due to subducting material (Maguire et al., 2018; Wang & He, 2020). We indicate examples of positive RF values below the 660-km discontinuity in Figure 3c and Figures S3, S4 & S5 in the Supporting Information S1. Since the remnant Farallon slab lies at MTZ depths in Yellowstone region, when identifying LVZs below the 660-km discontinuity we conservatively chose not to interpret negative signals directly below a sharp positive pulse, to avoid interpreting a side lobe.

Similar to the LVZs above the 410-km discontinuity, the subducting Farallon slab can displace hydrous MTZ rock into the lower mantle, where dehydration melting is generated. LVZs at ~750 km depth have been imaged in multiple regions of downwelling including the Japan subduction zone (Liu et al., 2016), central US (Schmandt et al., 2014), underneath the Alps (Liu et al., 2018), and Tibet (Panero et al., 2020). Underneath the western US, we find our RF imaging to agree most with Schmandt et al. (2014) in the northern portion of the station footprint. Since hydrous melt below the MTZ should be buoyant relative to the ambient mantle, another mechanism must be operating to generate melts ~100 km below the MTZ and keep them there. The two proposed mechanisms for hydrogen transport to ~750 km include free metallic iron (Liu et al., 2016) and the breakdown of hydrous garnet (Panero et al., 2020). Comparing these two models, the water capacity of garnet is very low even in a cold mid mantle (~1,430 ppm), though the mineral itself could be common in the assemblage. Metallic iron can hold up to 10 wt% water, so a small amount (0.1%) of metallic Fe can transport substantial amounts of water. Additionally, bridgmanite has been shown to hold at least ~1,020 ppm of water in laboratory experiments (Fu et al., 2019). A confident choice between these requires further investigation.

4.3. Conclusions and Future Work

The features of the middle mantle around Yellowstone hotspot are complex, but they show consistency with the MTZ water-filter hypothesis (Bercovici & Karato, 2003; Karato et al., 2020; Liu et al., 2016), in which mineral phase changes in convective mantle flows release water and encourage partial melting. High-frequency MTC RFs migrated to depths between 310 and 760 km have identified LVZs above and below the MTZ around the Yellowstone hotspot. No LVZs below the MTZ are detected where the plume is upwelling, as is anticipated by this model. We find that a depressed 410-km discontinuity and a shallowed 660-km discontinuity agree with geodynamics as extrapolated from tomographic images of the Yellowstone plume, suggesting a lower mantle origin. Surrounding the plume, we observe LVZs which may be generated when hydrous MTZ rock is transported out of the MTZ by the upwelling plume flow field.

Further work clarifying the stability of either metallic Fe (Liu et al., 2016) or hydrous garnet (Panero et al., 2020) in the uppermost lower mantle is necessary to understand better the mechanism transporting hydrogen to ~750 km depth. Mineral-physics experiments examining the wetting behavior of melts generated below the MTZ are necessary to improve the understanding of the seismic properties, because large dihedral angles would weaken the influence of melt on seismic wavespeeds. Further RF investigation of the 410-km discontinuity surrounding mantle plumes would provide more insight into potential entrainment of hydrous MTZ rock in mantle flow and associated partial melting. Such studies are difficult, due to poor seismic data coverage of mantle plumes. Additionally, more RF imaging of the western US is warranted to image slab remnants that may be descending through the MTZ, potentially causing LVZs above and below the MTZ. These further studies will allow for greater understanding of the solid-Earth water cycle and long-term ocean-mass regulation (Karato et al., 2020).

Data Availability Statement

Seismic data used in this research are available from the IRIS DMC repository (http://ds.iris.edu/ds/nodes/dmc/). All seismic data were recorded on the USArray Transportable Array with network code TA (http://www.usarray.org/researchers/data). Data can be accessed via SOD (http://ds.iris.edu/ds/nodes/dmc/software/downloads/sod/3-2-9/) or Irisfetch (http://ds.iris.edu/ds/nodes/dmc/software/downloads/irisfetch.m/2-0-11/). The US-SL-2014 tomography model used is available from the IRIS Earth Model Collaboration (http://ds.iris.edu/ds/products/emc/). Interpreted MTZ topography and LVZ location data is available on the Dryad data repository (https://doi.org/10.5061/dryad.zgmsbcccn).

Acknowledgments
This research was supported by NSF grant EAR-1764271. Comments from Mary Chen and Shun-Ichiro Karato benefitted the manuscript. We would like to thank editor Daoyuan Sun for his assistance with this manuscript. Comments from two anonymous reviewers allowed us to improve the manuscript significantly.

References

Bercovici, D., & Karato, S.-I. (2003). Whole-mantle convection and the transition-zone water filter. *Nature*, *425*(6951), 39–44. https://doi.org/10.1038/nature01918

Bianchi, I., Park, J., Piana Agostinetti, N., & Levin, V. (2010). Mapping seismic anisotropy using harmonic decomposition of receiver functions: An application to Northern Apennines, Italy. *Journal of Geophysical Research*, *115*, B12317. https://doi.org/10.1029/2009JB007061

Bina, C. R., & Helffrich, G. (1994). Phase transition Clapeyron slopes and transition zone seismic discontinuity topography. *Journal of Geophysical Research*, *99*(B8), 15853–15860. https://doi.org/10.1029/94JB00462

Bolfan-Casanova, N. (2005). Water in the Earth's mantle. *Mineralogical Magazine*, *69*(3), 229–257. https://doi.org/10.1180/0026461056930248

Christiansen, R., Foulger, G., & Evans, J. (2002). Upper-mantle origin of the Yellowstone hotspot. *The Geological Society of America Bulletin*, *114*(10), 1245–1256. https://doi.org/10.1130/0016-7606(2002)114<1245:UMOOTY>2.0.CO;2

Deuss, A., Redfern, S. A. T., Chambers, K., & Woodhouse, J. H. (2006). The nature of the 660-kilometer discontinuity in Earth's mantle from global seismic observations of PP precursors. *Science*, *311*(5758), 198–201. https://doi.org/10.1126/science.1120020

Dueker, K. G., & Sheehan, A. F. (1997). Mantle discontinuity structure from midpoint stacks of converted *P* to *S* waves across the Yellowstone hotspot track. *Journal of Geophysical Research*, *102*(B4), 8313–8327. https://doi.org/10.1029/96JB03857

Eagar, K. C., Fouch, M. J., & James, D. E. (2010). Receiver function imaging of upper mantle complexity beneath the Pacific Northwest, United States. *Earth and Planetary Science Letters*, *297*(1–2), 141–153. https://doi.org/10.1016/j.epsl.2010.06.015

Fee, D., & Dueker, K. (2004). Mantle transition zone topography and structure beneath the Yellowstone hotspot. *Geophysical Research Letters*, *31*(18), L18603. https://doi.org/10.1029/2004GL020636

Fu, S., Yang, J., Karato, S.-I., Vasiliev, A., Presniakov, M. Y., Gavriliuk, A. G., et al. (2019). Water concentration in single-crystal (Al, Fe)-bearing bridgmanite grown from the hydrous melt: Implications for dehydration melting at the topmost lower mantle. *Geophysical Research Letters*, *46*(10), 10346–10357. https://doi.org/10.1029/2019GL084630

Gilbert, H. J., Sheehan, A. F., Dueker, K. G., & Molnar, P. (2003). Receiver functions in the western United States, with implications for upper mantle structure and dynamics. *Journal of Geophysical Research*, *108*(B5), 2229. https://doi.org/10.1029/2001JB001194

Han, G., Li, J., Guo, G., Mooney, W. D., Karato, S.-I., & Yuen, D. A. (2021). Pervasive low-velocity layer atop the 410-km discontinuity beneath the northwest Pacific subduction zone: Implications for rheology and geodynamics. *Earth and Planetary Science Letters*, *554*, 116642. https://doi.org/10.1016/j.epsl.2020.116642

Hier-Majumder, S., & Tauzin, B. (2017). Pervasive upper mantle melting beneath the western US. *Earth and Planetary Science Letters*, *463*, 25–35. https://doi.org/10.1016/j.epsl.2016.12.041

Hirschmann, M. M. (2006). Water, melting and the deep-Earth H_2O cycle. *Annual Review of Earth and Planetary Sciences*, *34*, 629–653. https://doi.org/10.1146/annurev.earth.34.031405.125211

IRIS Transportable Array. (2003). *USArray Transportable Array*. International Federation of Digital Seismograph Networks. https://doi.org/10.7914/SN/TA

James, D. E., Fouch, M. J., Carlson, R. W., & Roth, J. B. (2011). Slab fragmentation, edge flow and the origin of the Yellowstone hotspot track. *Earth and Planetary Science Letters*, *311*(1–2), 124–135. https://doi.org/10.1016/j.epsl.2011.09.007

Jing, Z., & Karato, S. (2012). Effect of H_2O on the density of silicate melts at high pressures: Static experiments and the application of a modified hard-sphere model of equation of state. *Geochimica et Cosmochimica Acta*, *85*, 357–372. https://doi.org/10.1016/j.gca.2012.03.001

Karato, S. (2011). Water distribution across the mantle transition zone and its implications for global material circulation. *Earth and Planetary Science Letters*, *301*(3–4), 413–423. https://doi.org/10.1016/j.epsl.2010.11.038

Karato, S.-I., Karki, B., & Park, J. (2020). Deep mantle melting, global water circulation and its implications for the stability of the ocean mass. *Progress in Earth and Planetary Science*, *7*, 76. https://doi.org/10.1186/s40645-020-00379-3

Kennett, B. L. N., Engdahl, E. R., & Buland, R. (1995). Constraints on seismic velocities in the Earth using seismic traveltimes. *Geophysical Journal International*, *122*(1), 108–124. https://doi.org/10.1111/j.1365-246X.1995.tb03540.x

Kohlstedt, D. L., Keppler, H., & Rubie, D. C. (1996). Solubility of water in the α, β and γ phases of $(Mg, Fe)_2SiO_4$. *Contributions to Mineralogy and Petrology*, *123*(4), 345–357. https://doi.org/10.1007/s004100050161

Krischer, L., Megies, T., Barsch, R., Beyreuther, M., Lecocq, T., Caudron, C., & Wassermann, J. (2015). ObsPy: A bridge for seismology into the scientific Python ecosystem. *Computational Science & Discovery*, *8*(1), 14003. https://doi.org/10.1088/1749-4699/8/1/014003

Langmuir, C. H., & Broecker, W. S. (2012). *How to build a habitable planet* (2nd ed.). Princeton University Press.

Liu, Z., Park, J., & Karato, S.-I. (2016). Seismological detection of low-velocity anomalies surrounding the mantle transition zone in Japan subduction zone. *Geophysical Research Letters*, *43*(6), 2480–2487. https://doi.org/10.1002/2015GL067097

Liu, Z., Park, J., & Karato, S.-I. (2018). Seismic evidence for water transport out of the mantle transition zone beneath the European Alps. *Earth and Planetary Science Letters*, *482*, 93–104. https://doi.org/10.1016/j.epsl.2017.10.054

Long, M. D. (2016). The Cascadia Paradox: Mantle flow and slab fragmentation in the Cascadia subduction system. *Journal of Geodynamics*, *102*, 151–170. https://doi.org/10.1016/j.jog.2016.09.006

Maguire, R., Ritsema, J., & Goes, S. (2018). Evidence of subduction-related thermal and compositional heterogeneity below the United States from transition zone receiver function. *Geophysical Research Letters*, *45*, 8913–8922. https://doi.org/10.1029/2018GL078378

Nelson, P. L., & Grand, S. P. (2018). Lower-mantle plume beneath the Yellowstone hotspot revealed by core waves. *Nature Geoscience*, *11*(4), 280–284. https://doi.org/10.1038/s41561-018-0075-y

Ohtani, E., & Litasov, K. D. (2006). The effect of water on mantle phase transitions. *Reviews in Mineralogy and Geochemistry*, *62*, 397–420. https://doi.org/10.2138/rmg.2006.62.17

Panero, W. R., Thomas, C., Myhill, R., Pigott, J. S., Raepsaet, C., & Bureau, H. (2020). Dehydration melting below the undersaturated transition zone. *Geochemistry, Geophysics, Geosystems*, *21*, e2019GC008712. https://doi.org/10.1029/2019GC008712

Park, J., & Levin, V. (2000). Receiver functions from multiple-taper spectral correlation estimates. *Bulletin of the Seismological Society of America*, *90*(6), 1507–1520. https://doi.org/10.1785/0119990122

Park, J., & Levin, V. (2016). Statistics and frequency-domain moveout for multiple-taper receiver functions. *Geophysical Journal International*, *207*(1), 512–527. https://doi.org/10.1093/gji/ggw291

Park, J., Lindberg, C. R., & Vernon, F. L., III. (1987). Multitaper spectral analysis of high-frequency seismograms. *Journal of Geophysical Research*, *92*(12), 675–712 684. https://doi.org/10.1029/JB092iB12p12675

Pearson, D. G., Brenker, F. E., Nestola, F., McNeill, J., Nasdala, L., Hutchison, M. T., et al. (2014). Hydrous mantle transition zone indicated by ringwoodite included within diamond. *Nature*, *507*, 221–224. https://doi.org/10.1038/nature13080

Saal, A. E., Hauri, E. H., Langmuir, C. H., & Perfit, M. R. (2002). Vapour undersaturation in primitive mid-ocean-ridge basalt and the volatile content of Earth's upper mantle. *Nature*, *419*(6906), 451–455. https://doi.org/10.1038/nature01073

Schmandt, B., Dueker, K., Humphreys, E., & Hansen, S. (2012). Hot mantle upwelling across the 660 beneath Yellowstone. *Earth and Planetary Science Letters*, 331–332. https://doi.org/10.1016/j.epsl.2012.03.025

Schmandt, B., Dueker, K. G., Hansen, S. M., Jasbinsek, J. J., & Zhang, Z. (2011). A sporadic low-velocity layer atop the western U.S. mantle transition zone and short-wavelength variations in transition zone discontinuities. *Geochemistry, Geophysics, Geosystems*, *12*(8), Q08014. https://doi.org/10.1029/2011GC003668

Schmandt, B., Jacobsen, S. D., Becker, T. W., Liu, Z., & Dueker, K. G. (2014). Dehydration melting at the top of the lower mantle. *Science*, *344*, 1265–1268. https://doi.org/10.1126/science.1253358

Schmandt, B., & Lin, F. C. (2014). *P* and *S* wave tomography of the mantle beneath the United States, *Geophysical Research Letters*, *41*(18), 6342–6349. https://doi.org/10.1002/2014GL061231

Simmons, N. A., & Gurrola, H. (2000). Multiple seismic discontinuities near the base of the transition zone in the Earth's mantle. *Nature*, *405*, 559–562. https://doi.org/10.1038/35014589

Song, T.-R. A., Helmberger, D. V., & Grand, S. P. (2004). Low-velocity zone atop the 410-km seismic discontinuity in the northwestern United States. *Nature*, *427*, 530–533. https://doi.org/10.1038/nature02231

Tauzin, B., Debayle, E., & Wittlinger, G. (2010). Seismic evidence for a global low-velocity layer within the Earth's upper mantle. *Nature Geoscience*, *3*(10), 718–721. https://doi.org/10.1038/ngeo969

Trabant, C., Hutko, A. R., Bahavar, M., Karstens, R., Ahern, T., & Aster, R. (2012). Data products at the IRIS DMC: Stepping stones for research and other applications. *Seismological Research Letters*, *83*(5), 846–854. https://doi.org/10.1785/0220120032

Tschauner, O., Huang, S., Greenberg, E., Prakapenka, V. B., Ma, C., Rossman, G. R., et al. (2018). Ice-VII inclusions in diamonds: Evidence for aqueous fluid in Earth's deep mantle. *Science*, *359*, 1136–1139. https://doi.org/10.1126/science.aao3030

Wang, L. M., & He, X. B. (2020). Sharpness of the paired 660-km discontinuity beneath the Izu-Bonin area. *Earth and Planetary Physics*, *4*(6), 627–638. https://doi.org/10.26464/epp2020067

Wang, X., Chen, Q. F., Niu, F., Wei, S., Ning, J., Li, J., et al. (2020). Distinct slab interfaces imaged within the mantle transition zone. *Nature Geoscience*, *13*, 822–827. https://doi.org/10.1038/s41561-020-00653-5

Yang, J., & Faccenda, M. (2020). Intraplate volcanism originating from upwelling hydrous mantle transition zone. *Nature*, *579*, 88–91. https://doi.org/10.1038/s41586-020-2045-y

Yoshino, T., Nishihara, Y., & Karato, S.-I. (2007). Complete wetting of olivine grain boundaries by a hydrous melt near the mantle transition zone. *Earth and Planetary Science Letters*, *256*(3), 466–472. https://doi.org/10.1016/j.epsl.2007.02.002

Zhao, D., & Ohtani, E. (2009). Deep slab subduction and dehydration and their geodynamic consequences: Evidence from seismology and mineral physics. *Gondwana Research*, *16*(3–4), 401–413. https://doi.org/10.1016/j.gr.2009.01.005

Zhou, Y. (2018). Anomalous mantle transition zone beneath the Yellowstone hotspot track. *Nature Geoscience*, *11*, 449–453. https://doi.org/10.1038/s41561-018-0126-4